Available online at www.sciencedirect.com
ScienceDirect
Journal of Power Sources 161 (2006) 856–863
JOURNAL OF POWER SOURCES
www.elsevier.com/locate/jpowsour

Magnetic resonance imaging (MRI) of PEM dehydration and gas manifold flooding during continuous fuel cell operation

Kevin R. Minard, Vilayanur V. Viswanathan, Paul D. Majors, Li-Qiong Wang *, Peter C. Rieke *

Pacific Northwest National Laboratory, Richland, WA 99352, United States

Received 23 February 2006; received in revised form 26 April 2006; accepted 27 April 2006
Available online 6 June 2006

Abstract

Magnetic resonance imaging (MRI) was employed for visualizing water inside a proton exchange membrane (PEM) fuel cell during 11.4 h of continuous operation with a constant load. Two-dimensional images acquired every 128 s revealed the formation of a dehydration front that propagated slowly over the surface of the fuel cell membrane—starting from gas inlets and progressing toward gas outlets. After traversing the entire PEM surface, channels in the gas manifold began to flood on the cathode side. To establish a qualitative understanding of these observations, acquired images were correlated to the current output and the operating characteristics of the fuel cell. Results demonstrate the power of MRI for visualizing changing water distributions during PEM fuel cell operation, and highlight its potential utility for studying the causes of cell failure and/or strategies of water management.

Keywords: PEM; Fuel cell; Dehydration; Flooding; MRI

1. Introduction

Proton exchange membrane (PEM) fuel cells produce liquid water as a byproduct of electrical power generation, and their optimal performance generally requires a delicate balance between water formation and removal as both dehydration and/or flooding hinder mass transport to reactive catalytic sites. Excess water build up, on one hand, prevents sufficient gas supply, whereas poor water retention reduces ionic conductivity. Water management seeks to balance water production with removal by understanding the relevant transport processes [1,2], and exploits their impact on water distribution [3] to optimize electrochemical function [4].

During PEM fuel cell operation, water is normally found in gas supply channels, the membrane itself, and throughout both catalyst and gas diffusion layers. It is uncertain, however, how the amount of water in each location is affected by different operating conditions or how corrective actions potentially help water balance in one region and not another. To clarify these issues, optical and neutron-based imaging studies have both been reported for visualizing water inside PEM fuel cells. Optical techniques are, however, limited by the opaque nature of fuel cell components [5–7], and neutron imaging only provides three-dimensional (3D) information if a series of 2D images are acquired using different exposure angles. Since multiple exposures require more time, neutron imaging is most often applied using a single exposure for fuel cell research [8–10], but in this case, the precise location of water is difficult to determine since overlapping layers are not depth-resolved [8]. Furthermore, appropriate neutron sources are only available at a handful of research facilities so their widespread utilization is impractical.

Compared with either optical or neutron-based methods, magnetic resonance imaging (MRI) is widely available, inherently three-dimensional, and capable of visualizing water in opaque structures. In recognition of these attributes, MRI has been successfully exploited for visualizing water inside operating PEM fuel cells [11,12], for observing membrane dehydration [13], understanding the effects of membrane thickness on cell performance [14], and to assess new strategies for water management [15]. To obtain optimal MRI performance, prior studies have exploited specially designed, non-commercial fuel cells since conductive components absorb the incident radio-frequency (RF) energy required for image generation, and

* Corresponding authors. Tel.: +1 509 375 2078; fax: +1 509 375 2186.
E-mail addresses: lq.wang@pnl.gov (L.-Q. Wang), peter.rieke@pnl.gov (P.C. Rieke).

0378-7753/$ – see front matter © 2006 Elsevier B.V. All rights reserved.
doi:10.1016/j.jpowsour.2006.04.125

strongly magnetic (ferromagnetic and paramagnetic) materials can introduce image artifacts [12]. Here, the limitations imposed by fuel cell materials are examined, methods are described for minimizing their adverse effects on image quality, and MRI is utilized for visualizing membrane dehydration and gas manifold flooding during continuous PEM fuel cell operation. Overall, results further demonstrate MRI's potential as a diagnostic tool for visualizing water distribution inside operating PEM fuel cells, and provide a basis for assessing the feasibility of industrial applications involving commercial cells or stacks.

2. Materials and methods

2.1. Fuel cell design, construction, and operation

It is well recognized that the distribution of water within an operating fuel cell is ultimately affected by its design, construction, and operation. Fig. 1 shows a schematic of the MRI-compatible fuel cell used in the current study. Its overall size is significantly smaller than a typical commercial device and is limited by the available space inside the imaging magnet that was employed. Constructed from polyetheretherketone (PEEK), the fuel cell consists of a 2.54 cm diameter body that holds gas manifolds, gas diffusion layers (Model B-1, carbon cloth design A with standard wet proofing, E-TEK Division, PEMEAS Fuel Cell Technologies**,** Somerset, NJ), and a three-layer membrane electrode assembly (MEA). The MEA was commercially available, and utilizes a Nafion-N117 membrane with 0.3 mg Pt cm^{-2} (Ion Power, New Castle, DE). The active area of the electrodes is 1.7 cm^2, and electrical contact is achieved using copper wire leads connected to gold-coated PEEK gas manifolds. Since the copper wire was not in direct contact with any part of the MEA, degraded performance from copper ions was avoided. Further, use of an MEA with a relatively thick Nafion membrane was chosen to avoid rapid dehydration.

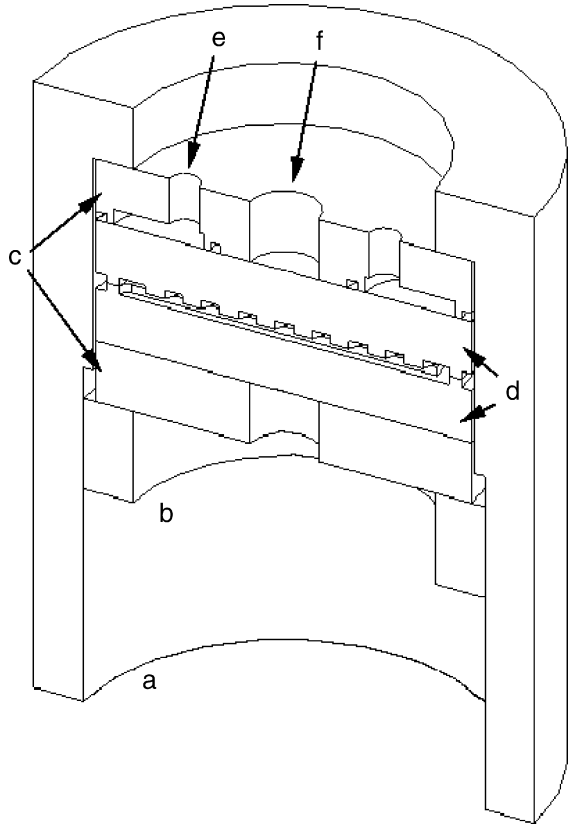

Fig. 1. Schematic representation of fuel cell fixture used in MRI experiments. All parts were machined from PEEK. The parts are: (a) 2.54 cm diameter main fixture body, (b) threaded ring for retention of and applying pressure to the manifold and MEA, (c) manifold interface fixtures, and (d) gold-coated manifold with serpentine pattern shown in Fig. 3a. Prior to operation the MEA and gas diffusion layers are placed between gold-coated gas manifolds (d) along with appropriate o-rings for sealing. A copper conductor provides external electrical contact to the gas manifold through the tapped center holes (f). Gas inlet and outlet lines were glued to the smaller holes (e) in the manifold interface.

Compared with a commercial fuel cell, the design depicted in Fig. 1 is relatively simple and seeks to limit use of conducting and/or magnetic materials since these can adversely affect image quality. The precise limitations imposed by fuel cell materials on MRI experiments remains uncertain, however, and no consensus regarding the feasibility of imaging commercial devices without material modification yet exists. Therefore, a goal of the current study was to exploit the relatively simple design depicted in Fig. 1 to better understand these issues. In this context, the fuel cell used here was not meant to be representative of a commercial device nor was its performance rigorously optimized. Rather, it was used to define achievable imaging performance, assess limitations imposed by fuel cell materials, and provide data that could then be used to examine the feasibility of exploiting MRI for the diagnostics of commercial devices.

During operation at room temperature inside the imaging magnet, hydrogen in argon (2.8%) was used as the anode fuel and a simple aquarium pump provided air to the cathode. Gas flows were controlled by Rotameter^{TM}, variable-area flow meters (Cole-Palmer Instrument Company, Vernon Hills, IL) and humidified at room temperature using a fine glass frit laboratory bubbler with a 20 cm water column. During imaging, a constant load of 12.2 Ω (metal film resistor) was used to control cell current and voltage. The flow of hydrogen/argon (on the anode side) and air (on the cathode side) were 12 and 45 ml min^{-1}, respectively. Depending on the current, the flow rate of hydrogen fuel corresponded to 1.2–4× stoichiometric units. Due to un-optimized seal design, the air flow rate had to be of the same order of magnitude as the fuel flow rate in order to obtain a stable open circuit voltage. Hence, the use of dilute H_2 in the anode stream necessitated a high cathode air stoich. To examine whether the high flow rates affected water distribution, MRI was first used to visualize water within the fuel cell for six ours prior to connecting the 12.2 Ω load. Importantly, during this initial testing, no membrane dehydration or channel flooding occurred. Gas humidification was therefore sufficient to maintain stable membrane hydration in the absence of electrochemical activity, and any residual fuel crossover was not significant enough to cause channel flooding.

2.2. Magnetic resonance imaging

Proton (^{1}H) magnetic resonance (MR) imaging was performed at 11.7 T (500 MHz) using an Avance imaging spectrom-

eter (Bruker Instruments, Fremont, CA) equipped with an 89-mm-diameter, vertical-bore magnet (Magnex Scientific, Oxford, UK). All electrical connections to the fuel cell were shielded with grounded metal braiding so that the long leads (required for operation inside the magnet bore) would not act like antennas and transmit unwanted radio-frequency (RF) interference from outside the magnet into the imaging system's sensitive RF receiver. For imaging, the fuel cell assembly was placed inside a Bruker birdcage resonator that was used for exciting and receiving the 500 MHz ^{1}H NMR signal. The resonator had an internal clearance parallel with the magnet bore that was just large enough to accommodate the cylindrical shape of the fuel cell assembly (see Fig. 1). In this configuration, the resonator's RF field was aligned perpendicular to the fuel cell's central (symmetry) axis and was not significantly screened from its interior by gold-coated gas manifolds. Conceptually, significant RF screening by the conductive gas manifolds was avoided by minimizing the amount of field (i.e. flux) passing through their cross-section. Importantly, the same approach has been effective for imaging liquids between closely spaced, highly conductive, thick copper electrodes with large surface areas [16]. In this context, the dissipation of incident RF in the conducting current collection plates appears to be a surmountable obstacle for MRI. Particularly, since data here and elsewhere shows unambiguously that simple alignment of the RF field is effective for imaging materials sandwiched between planar conductive materials.

Perhaps more challenging than RF screening are the magnetic field distortions induced by differences in the volume magnetic susceptibility (χ_v) of nearby fuel cell materials. Particularly, since off-resonant water can contribute to a variety of image artifacts, including intensity variations caused by excitation and refocusing errors [17], poor slice localization [18], and spatial misregistration along the frequency-encode axis [19]. To optimize image quality in the current study, field heterogeneity in the plane of a fully hydrated Nafion-117 membrane was measured using the two-dimensional (2D), spin–echo sequence shown in Fig. 2. The sequence employed a single frequency-selective, 90° RF excitation together with a broadband, slice-selective, 180° refocusing pulse so images acquired using different carrier frequencies could be used to visualize the location of nuclei resonating in different static magnetic fields [19,20]. Results indicated that resonant membrane water spanned ~4500 Hz (or ~9.0 ppm) at 500 MHz.

In order to visualize *all* water inside the operating fuel cell, irrespective of resonance frequency, acquisition parameters for the sequence shown in Fig. 2 were optimized for the measured field heterogeneity. To minimize errors in slice localization and artifacts caused by off-resonant RF pulses, a 10 kHz bandwidth was utilized for both RF excitation and refocusing. Similarly, misregistration errors along the frequency encode axis (of MR images) were minimized by exploiting a maximum receiver bandwidth of 200 kHz. Raw 2D image data showing a square field-of-view (FOV) that was 3.5 cm on a side was then collected on a 64 × 64 matrix using four averages, an echo-time (TE) of 1.6 ms, a repetition time (TR) of 500 ms, and a 4-millimeter-thick slice that contained both the MEA and gas

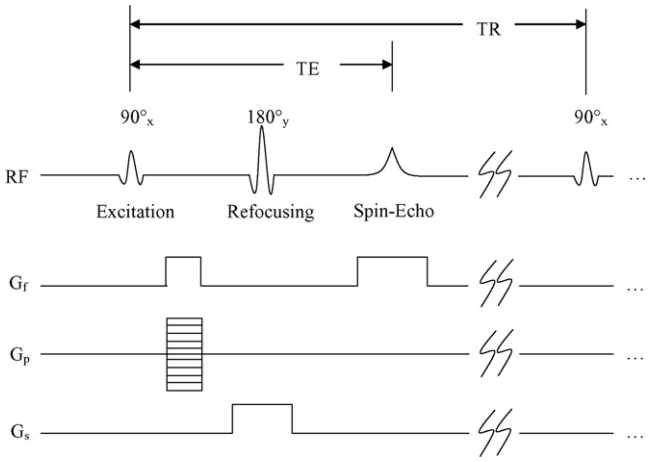

Fig. 2. The 2D spin–echo imaging experiment. The 90° RF pulse excites a region of the ^{1}H NMR spectrum centered at the carrier frequency. Then, the broadband 180° RF pulse refocuses the signal within a chosen slice to form a spin–echo at a time TE after excitation. At the same time, pulsed magnetic field gradients (G) are applied along three orthogonal axes to select signal from the chosen slice (G_s) and to encode (G_p and G_f) spatial information within the excited plane. The entire pulse sequence is then repeated with a fixed repetition time (TR) to accumulate image data acquired with different phase-encoding gradient values (G_p). During each repetition, time-domain ^{1}H NMR data is acquired during the last frequency encoding gradient pulse (G_f) at the time of spin–echo formation.

delivery channels. Each 2D image therefore had a planar resolution of 550 μm, only required 128 s to collect, and provided a comprehensive view of the fuel cell's interior. To study temporal changes, 2D data collection was repeated 320 times, every 128 s, over 11.4 h of continuous fuel cell operation, and afterward, each 2D image was Fourier reconstructed on a 512 × 512 matrix.

3. Results

Magnetic resonance imaging in high static magnetic fields offers the potential for a more detailed view of water inside operating PEM fuel cells since MR sensitivity generally increases with static field strength [19]. A potential shortcoming, however, is that the field heterogeneity induced by differences in the volume magnetic susceptibility (χ_v) of nearby fuel cell materials also increases and this can degrade overall image quality if acquisition parameters are not appropriately optimized.

In the current study, the 2D spin–echo experiment in Fig. 2 was initially employed for imaging a fully hydrated, Nafion-117 membrane, and results were exploited for measuring the field shifts induced by nearby fuel cell materials. Inside the fuel cell, the membrane was sandwiched between opposing gas manifolds as depicted in Fig. 1. To reduce variations in magnetic susceptibility for MR studies, gas manifolds on opposite sides were oriented so machined gas-flow channels overlapped as much as possible. Ignoring the thin layer of gold used to coat the manifold surfaces, the majority of membrane water was therefore located either between air or PEEK interfaces. Fig. 3a shows the gas channels in the fuel cell manifold and reflects the membrane regions contacted by either PEEK or air. Since the volume magnetic susceptibility (χ_v) for both differ by about 9.0 ppm [21],

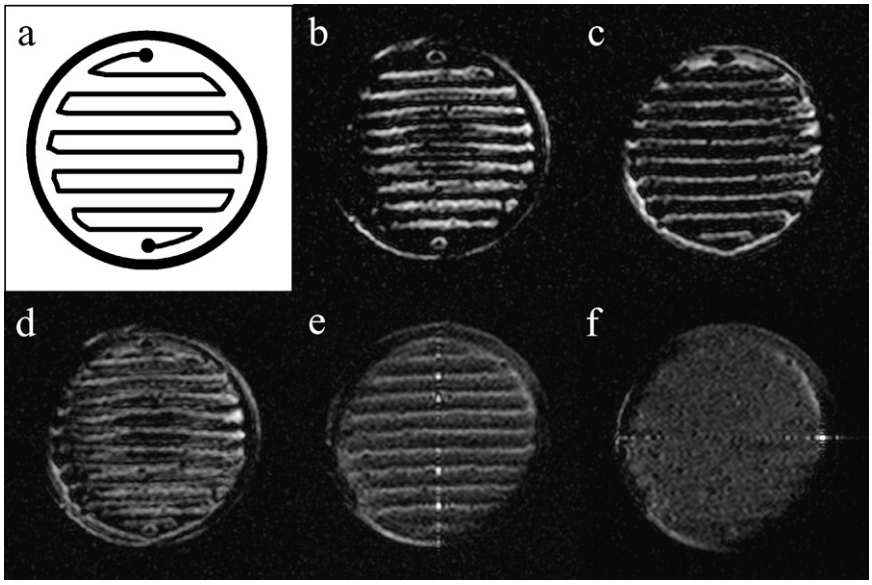

Fig. 3. Imaging optimization and characterization of static field heterogeneity. (a) Schematic representation showing the pattern of milled channels in one of the gold-coated gas manifolds. When sandwiched between two identical pieces water in the Nafion-117 membrane is located either between air (black) or PEEK (white) interfaces. Differences in the volume magnetic susceptibility then shift the resonance frequency of membrane water depending on its location. (b) MR image of water in a 500 Hz band near the shift anticipated when molecules are sandwiched between apposing air interfaces. (c) MR image of water in a 500 Hz band near the shift anticipated when molecules are sandwiched between apposing PEEK interfaces. (d) Overlay of (b and c). (e) MR image acquired when the bandwidth of applied RF is greater than the frequency range spanned by resonating membrane water, and frequency encoding (G_f, cf., Fig. 2) is applied in the vertical direction. (*f*) Same as (e)) except frequency encoding is along the horizontal direction.

membrane water molecules were anticipated to resonate over a range of frequencies that is predicted to be about ~4500 Hz wide at 500 MHz.

Anticipated magnetic field heterogeneity is confirmed by MR images in Figs. 3b–f. Fig. 3b, for example, shows the location of water in a 500 Hz band near the field shift expected when molecules are sandwiched between opposing air interfaces. Comparison with Fig. 3a shows that membrane water is not observed near the turns of the flow channels in the gas manifold. In principle, this is because anode and cathode-side manifolds are identical. Consequently, when facing towards one another in the assembled fuel cell (cf., Fig. 1), the turns on each manifold do not overlap. Membrane water near the turns is therefore sandwiched between air on one side, and PEEK on the other. Thus, water in those locations resonates at a different frequency. Other differences with Fig. 3a (like the small curvature of the horizontal channels) are due to the larger-scale heterogeneity of the imaging magnet's static field. These static field shifts are, however, relatively small and the dominant features seen in Fig. 3b are attributable to local variations in the magnetic susceptibility of fuel cell materials. This notion is further strengthened by Fig. 3c. It shows the spatial distribution for water near the resonance frequency expected when membrane water is between opposing PEEK interfaces. Comparison with Fig. 3a shows that the vast majority of observed features correspond with the overlapping lands on the gas manifold. Fig. 3d shows the overlay of Fig. 3c with Fig. 3b and illustrates how more membrane water is observed by exciting over a broader range of resonance frequencies. This is confirmed in Fig. 3e which shows a single MR image acquired when the bandwidth of applied RF is greater than the frequency range spanned by resonating membrane water. Errors in RF excitation, refocusing, and slice localization are therefore minimized. Nevertheless, while more water is observed in a single data acquisition, its overall distribution still appears non-uniform and image intensity is severely modulated in the frequency-encoded (vertical) direction.

Differences in water resonance frequency are predicted to cause a vertical misregistration of approximately 6 pixels (or roughly 400 μm) in Fig. 3e. This is based on the anticipated frequency spread of 4500 Hz for resonant water molecules in the Nafion-117 membrane, the reconstructed matrix dimension along the (vertical) frequency encode axis (512), the acquisition bandwidth (200,000 Hz), and a factor of 1/2 that results from centering the carrier frequency, such that 6 ~$0.5 \times 4500 \times 512/200{,}000$. In this context, the light and dark regions of image intensity arise because regions of water between air are spatially shifted one way and regions between PEEK are shifted the other. Since flow channels in the gas manifold are primarily horizontal (cf., Fig. 3a), misregistration artifacts can be minimized by placing the frequency-encoded axis of the image parallel with the main (horizontal) gas channels. In this case, all susceptibility-induced shifts along the frequency-encoded axis are towards the periphery of the membrane where no signal exists to cause bright overlaps. As shown in Fig. 3f, this simple procedure then yields an MR image with substantially improved uniformity.

After imaging optimization, the fuel cell was reassembled with both gas diffusion layers and the MEA. Fig. 4 shows the cell current density and power output under the specified operating conditions in the magnet bore. It is seen that our particular cell did not show the classical activation, resistive and mass transport dominated polarization curve regions. The open cir-

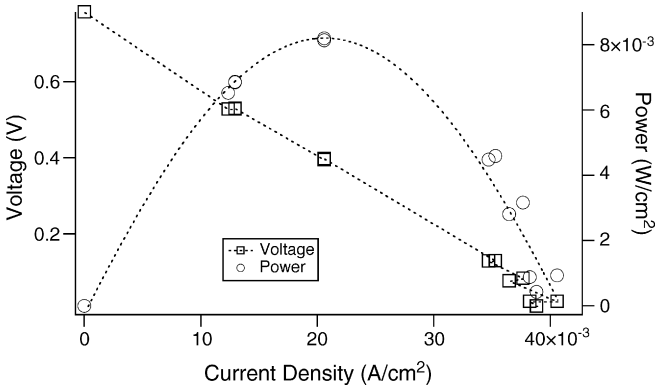

Fig. 4. Current–voltage and power data for the fuel cell just prior to MR image acquisition over 11.4 h of continuous operation. The dashed power curve line is a visual fit only to clarify the data trends.

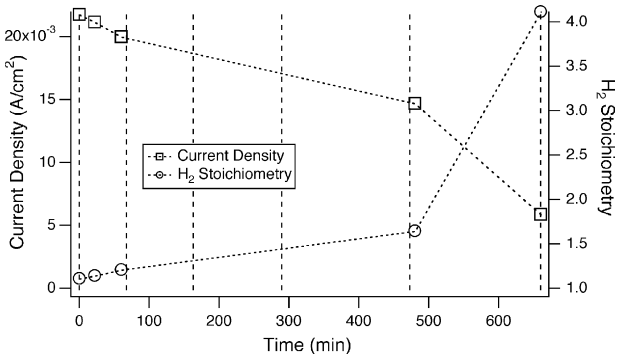

Fig. 5. Current and hydrogen utilization over 11.4 h during the acquisition of MR images shown in Fig. 6. The images there were acquired at 0, 66, 164, 290, 473, and 678 min, and these times are denoted in the figure as short-dashed lines.

cuit potential was also low and depended on flow rates (data not shown). Inadequate seals are therefore the most likely reason why the current density and power output were not comparable to commercially available PEM power supplies. However, our purpose was not to optimize cell performance at this stage but rather to utilize MRI to monitor and visualize cell performance as degradation occurs.

Fig. 5 shows the current density and hydrogen stoichiometry over 11.4 h of continuous operation with a constant load. Current measurements were taken manually and as the experiment was run overnight data was not acquired the entire time. Data in Fig. 5 therefore highlights overall performance trends. In addition, it is noted that hydrogen utilization is just the inverse of H_2 stoichiometry. The increase in stoichiometry that is depicted near the end of operation in Fig. 5 therefore indicates a dramatic decrease in hydrogen utilization. To understand observed changes in electrochemical performance, Fig. 6 shows representative images of the PEM fuel cell acquired over the entire period of operation. Each image is from a series of 320 that were assembled into a continuous movie. The movie, condensed to a total viewing time of ∼1 min, is available from the authors. It is emphasized that the stills presented in Fig. 6, while representing the essence of the results, cannot convey, like the continuous movie does, the ebb and flow of water in the operating fuel cell.

Fig. 6a was acquired just prior to shunting the cell across the constant load and depicts the starting water distribution. Importantly, images collected over a 6-h period prior to shunting looked identical during initial testing under otherwise identical conditions; thereby, indicating a stable starting water distribution was achieved. During this setup period, the cell load (of 12.2 Ω) was chosen to induce a current near the power peak seen in Fig. 4 and, as discussed below, operation with this load

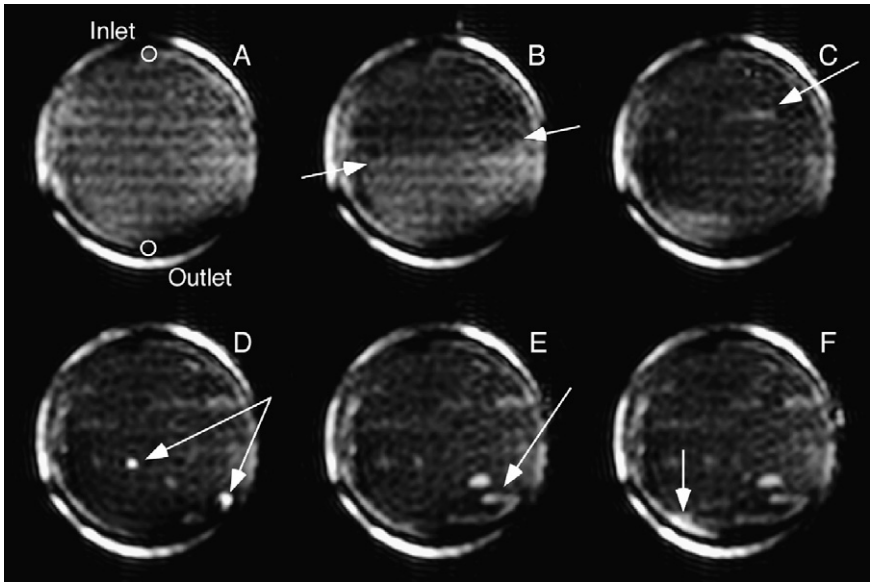

Fig. 6. Selected MR images showing water in an operating fuel cell over an 11.4-h period. Images were acquired at: (a) the start of the experiment and after (b) 66, (c) 164, (d) 290, (e) 473, and (f) 678 min. The fuel and oxidant inlet and outlet positions are labeled and the arrows in (b) highlight the position of the dehydration front that moved from the inlet towards the outlet. The grey scale was chosen to highlight the dehydration front formation and the actual signal intensity varied by approximately 10%. Regions showing flooding are also highlighted by white arrows. Images were obtained every 128 s and the full set of 320 images was assembled into a continuous movie that is available from the authors.

then led to an unstable distribution of water during continuous electrochemical operation.

Generally, the images in Fig. 6 show some intensity variations around the fuel cell's perimeter; presumably, because the MEA was not perfectly round and bunched slightly at the edges. The shape of the serpentine channels in the gas manifold is also evident and likely reflects variations in water content caused by squeezing the MEA tightly between opposing faces of the gas manifolds to increase contact pressure. Given these variations only a change in brightness can be interpreted as a change in water content. The precise amount, however, is difficult to determine since image data was acquired with a short repetition time (TR), and in this case, the image intensity depends on both the amount of water as well as its T_1-relaxation time [19]. In practice, this confounds the quantification of absolute water content since T_1 differs for bulk and membrane water, and varies with membrane hydration level [12]. Consequently, while a change in image intensity observed here reflects a change in water content, the actual amount requires a more rigorous analysis that accounts for the so-called T_1-weighting of acquired image data. Conversely, if imaging was performed more slowly using a longer TR, T_1-relaxation becomes inconsequential and data is then directly proportional to water content only. For this reason, previous MRI work typically employs longer TR's of a few seconds. Here, however, the goal was not to quantify absolute changes in water concentration but to visualize them as quickly as possible.

After shunting, the initial current density through the fuel cell was $\sim$22 mA cm^{-2} and the image did not change substantially for several minutes until a distinct front of dehydration in the MEA became visible. Generally, this was not anticipated and the operating conditions were not specifically designed to produce this effect. Nevertheless, the front's formation and propagation was clearly observed as a region of diminished intensity that started at the gas inlet (at the top of the image) and moved steadily with time down the entire face of the MEA. The image in Fig. 6b was acquired after 66 min of operation when the front was located about midway between gas inlet and outlets. By then, the current density had diminished to $\sim$19 mA cm^{-2} (cf., Fig. 5). The images show that water content decreased above the front (indicated by the arrows in Fig. 6b) but remained constant below it. Throughout this dehydration process the front remained clearly visible and moved steadily within the plane of the MEA.

It is noted that the grey scale used to present the images of Fig. 6 was adjusted to help visualize the front and the difference in water content it produced. Quantitative image analysis shows that image intensity decreased above the front by only 10%. It is therefore emphasized that the membrane did not completely dehydrate, and the clear visualization of the front demonstrates the ability to follow subtle changes in membrane hydration with MRI. Since no comparable changes were observed during initial testing with no load but otherwise identical operating conditions, the subtle variations in membrane hydration produced by the front are the direct result of the fuel cell's electrochemical function. Given the small changes in image intensity observed as the front propagated, it is perhaps not surprising that fuel cell's current density remained relatively constant (cf., Fig. 5).

After 164 min the image in Fig. 6c shows that the front had moved near the gas outlets and water now appeared in the gas manifold behind the front, (marked by an arrow). This was bulk water that had partially flooded the gas channel. The signal intensity directly adjacent to the channel flooding showed no change indicating that the bulk water did not rehydrate the membrane.

After 290 min of operation, Fig. 6d shows that the dehydration front completely disappeared and Fig. 5 shows that the current began to decrease more rapidly. The onset of manifold flooding is also evident as very bright spots marked in the image. The flooding observed earlier nearer the top of the images (cf., Fig. 6c) remains constant and, in comparison, the image brightness is much less than observed for the newly developed flood zones. At 473 min (Fig. 6e) the gas manifold flooding was seen to take the shape of the machined pathways in the manifold, and the cell current density had decreased to 16 mA cm^{-2}. Some areas appear brighter and are presumably more obstructed than others.

During the final hour of imaging (Fig. 6f) water was observed to accumulate near the edge of the gas manifold, close to the gas outlets (see white arrow). This is somewhat obscured by the poor uniformity of image intensity near the perimeter of the fuel cell but is clearly discerned by comparing the intensity in the vicinity of the white arrow, and noting the change from image to image. Unlike previous zones of flooding described above, the change in water signal located near the edge of the fuel cell is well outside the main flow channels that are machined in the gas manifold (cf., Fig. 3a). One possible explanation for this is that the previously flooded areas have blocked those main gas flow paths and the new flood zone is associated with gas flow that bypasses the obstructed regions. The obstructions therefore apparently do not lead to a build up of pressure that "blows" the manifold channels clear, and gas appears to preferentially flow around these areas through the gas diffusion layer. This is clearly seen in the movie of time-resolved MRI data where the water located in blocked flow channels (cf., white arrow in Fig. 6e) is seen to remain constant as the intensity near the arrow in Fig. 6f increases. During these changes, Fig. 5 shows that the current density was not zero but had decreased to 9 mA cm^{-2}.

4. Discussion

In this study, a front of partial dehydration was observed to propagate across the plane of the membrane electrode assembly (MEA), starting from the gas inlets and ending at the gas outlets. At the same time, cell current density gradually decreased by about 14%. The data therefore suggest that the partially dehydrated region above the front supported less current density (by about 14% on average) than the more hydrated region below. One possible explanation for the front's formation can be postulated based on the following observations. First, behind the front, imaging data shows that the MEA was partially dehydrated and therefore likely to be electrochemically impaired. Second, because the fuel cell was initially operating at about 80% utilization, the hydrogen may have been substantially depleted on

the outlet side of the front. Both factors might therefore have contributed to decreased electrochemical activity forward and behind the dehydration front. In this scenario, localized resistive heating along the front is a plausible mechanism for MEA dehydration.

The image in Fig. 6e shows the onset of localized flooding that diverts the gas flow paths. By analysis of the symmetry of the flooded gas pathways, and knowledge of the viewpoint of MR imaging, the flooding was determined to occur on the cathode side. This is as expected from the electroosmotic drag of water from anode to cathode. During the first 2 h of operation when the dehydration front formed and moved towards the gas outlet, the current density decreased by about 14% from 22 to 19 mA cm^{-2}. Conversely, over the final $3\frac{1}{2}$ h when flooding effects were apparent, the current density decreased an additional 60% from ~16 to 6 mA cm^{-2}. Since cell current density decreased slowly prior to this flooding and decreased more rapidly after, flooding and gas diversion appear to be more damaging in the current study than the initial MEA dehydration.

Although it is impossible to tell from these initial results if dehydration is more prevalent on the anode or cathode side, Tsushima et al. have employed thick imaging slices for visualizing the 2D distribution of water across the PEM, and have shown preferential dehydration on the anode side arising from electroosmotic drag [13]. If this is the case in this work, then flooding of the cathode seems to be a more important factor in degrading the current density than is anode-side dehydration.

In the current study, channel flooding seemed to occur after partial dehydration of the MEA. Flooding did not occur, for example, where the MEA was hydrated but onset shortly after the front passed. This suggests that the two phenomena are not independent but may occur in concert and lead to rapid cell failure. Nevertheless, the precise reason why flooding occurred after membrane dehydration remains unclear, especially since the dropping current density during membrane dehydration would result in the production of less water. One possible explanation is that once the dehydration front had passed from inlet to exit, the fuel cell was subjected to high current density near the exit, which then resulted in higher water production in that location. A secondary explanation could be formation of pinholes in the membrane due to dehydration, which can contribute to water generation by the direct reaction of H_2/O_2 on the Pt catalyst. More detail studies would, however, be required to establish such a mechanistic understanding and are outside the scope of the current work.

Taken together, results from this study and those from Tsushima et al. suggest that water distribution within the PEM is generally a four-dimensional function of space and time. Temporally resolved, 3D image data is therefore desirable for achieving a comprehensive understanding of water transport during fuel cell operation. This, however, is technically challenging. Suppose, for example, that one wanted 2D images of five *different* slices across the PEM used in the current study. In this case, each would show the water distribution across a different plane so changes in membrane dehydration from the anode to cathode could be assessed slice by slice. Unfortunately, if the same planar resolution (of 550 μm) was required, the signal-to-noise ratio (SNR) for membrane water in each slice would necessarily be five times lower since each slice would contain roughly 1/5 the water. Consequently, to achieve the same SNR as the current study, 2D, multi-slice, image data would need to be collected using 25 times more averages since the SNR for MRI only increases with the root of the number of averages [19]. The total acquisition time for each image would then be 25 × 128 s, or just less than an hour. Conversely, if planar resolution were increased to about a millimeter, water in each resolved volume increases by a factor of 4 and a temporal resolution near 128 s could then be maintained for a courser, 2D, multi-slice, MRI acquisition defined by an acceptable SNR. In this regard, the timely acquisition of 3D, MRI data is feasible but only if some compromise in spatial resolution is ultimately made. By comparison, a 2D neutron image requires 2 s to acquired and download, and planar resolution is typically about 160 μm [8]. However, data is not depth-resolved and information about water in different layers requires a 3D acquisition that can take minutes to hours to complete [8]. Multi-slice MRI may therefore provide more rapid 3D visualization, albeit, with courser resolution.

Beyond issues important for water management, MR imaging results in this study show that the water inside operating PEM fuel cells spans a range of resonance frequencies determined by susceptibility-induced magnetic field shifts. Findings also illustrate how imaging parameters must be optimized to minimize associated artifacts. Furthermore, since susceptibility induced magnetic field shifts vary linearly with magnetic field strength [19], results provide a quantitative basis for estimating the field-dependence of imaging performance in fuel cell applications. This is especially useful considering that the cost of MRI systems decreases dramatically with lower static field strengths.

To examine the feasibility of low-cost MRI for fuel cell applications it is helpful to consider how the signal-to-noise ratio (SNR) in an acquired image varies with static field strength. In the experiment depicted by Fig. 2, the image SNR varies with the resolved volume of the sample (voxel) and increases approximately linearly with static field strength when susceptibility-induced field distortions represent the dominant broadening mechanism and RF losses are mainly due to the resistance in the receiver coil [19]. Consequently, images with the same SNR as those in Fig. 6 could be acquired at 0.2 T if each resolved volume of the sample (voxel) were increased by approximately 11.7/0.2 or ~59. Assuming the same slice thickness, this scaling relationship then dictates that a planar resolution of 3.8 mm could be obtained in only 128 s at 0.2 T. Particularly, since resolution in this study was 0.55 mm at 11.7 T, and this must be multiplied by $\sqrt{59}$ to linearly scale each planar dimension and achieve the same SNR at 0.2 T. While spatial resolution of a few millimeters is not high it may be sufficient for diagnostics on larger fuel cells with larger, unobstructed regions. Of course, if greater heterogeneity requires better spatial resolution then some temporal resolution can be sacrificed as already discussed.

Conceptually, imaging at lower field strengths does offer some distinct advantages even though MRI sensitivity is necessarily reduced. RF penetration, for example, increases inversely with the square of the magnetic field strength [22]. Consequently,

at lower static field strengths, increased RF penetration in conducting materials opens the possibility of visualizing water gradients *inside of* the porous carbon layers rather than only between or outside conducting current collectors. Likewise, since the field variations induced by differences in magnetic susceptibility decrease linearly with static field strength [19], image artifacts stemming from off-resonance water in close proximity with fuel cell materials are significantly reduced. Moreover, such low field systems are commercially available at low-cost, are portable, and have an open geometry that can potentially accommodate a commercial fuel cell stack [23]. One may therefore envision multi-slice MRI of a commercial stack at low fields where increased RF penetration and reduced susceptibility broadening eliminates the need for any material modifications. Tradeoffs between magnetic field strength and cost with achievable imaging performance are therefore important to consider for potential industrial applications.

5. Conclusions

Magnetic resonance (MR) imaging was used to follow water distribution in a small fuel cell over 11 h of continuous operation and results were correlated with concurrent electrical measures of cell performance. The work demonstrates the utility of MRI for visualizing water non-uniformity across the face of the MEA and understanding fuel cell performance in terms of water management. In this study, however, no attempt was made to systematically study alternative methods for maintaining optimal water balance or to optimize cell design. Nevertheless, valuable insight was gained into possible failure mechanisms simply by visualizing water distribution and correlating imaging results with total cell current. It is this elegant simplicity that ultimately underlies MRI's utility as a diagnostic tool for fuel cell research and will undoubtedly stimulate its wider use for related applications.

Acknowledgements

Research was performed in part in the Environmental Molecular Science Laboratory (a national scientific user facility sponsored by the US Department of Energy's Office of Biological and Environmental Research) located at Pacific Northwest National Laboratory (PNNL), and operated for DOE by Battelle. Financial support provided by the Laboratory Directed Research and Development (LDRD) program.

References

[1] G. Karimi, X. Li, Electroosmotic flow through polymer electrolyte membranes in PEM fuel cells, J. Power Sources 140 (2005) 1–11.
[2] H. Sun, H. Liu, L.-J. Guo, PEM fuel cell performance and its two-phase mass transport, J. Power Sources 143 (2005) 125–135.
[3] S. Shimpalee, S. Greenway, D. Spuckler, J.W. Van Zee, Predicting water and current distributions in a commercial-size PEMFC, J. Power Sources 135 (2004) 79–87.
[4] T.V. Nguyen, M.W. Knobb, A liquid water management strategy for PEM fuel cell stacks, J. Power Sources 114 (2003) 70–79.
[5] K. Tüber, D. Pócza, C. Hebling, Visualization of water buildup in the cathode of a transparent PEM fuel cell, J. Power Sources 124 (2003) 403–414.
[6] K. Sugiura, M. Nakata, T. Yodo, Y. Nishiguchi, M. Yamauchi, Y. Itoh, Evaluation of a cathode gas channel with a water absorption layer/waste channel in a PEFC by using visualization technique, J. Power Sources 145 (2005) 526–533.
[7] H.-S. Kim, T.-H. Ha, S.-J. Park, K. Min, M. Kim, Visualization study of cathode flooding with different operating conditions in a PEM unit fuel cell, in: Proceedings of FUELCELL2005, The Third International Conference on Fuel Cell Science, Engineering and Technology, Ypsilanti, Michigan, May 23–25, 2005.
[8] R. Satija, D.L. Jacobson, M. Arif, S.A. Werner, In situ neutron imaging technique for evaluation of water management systems in operating PEM fuel cells, J. Power Sources 129 (2004) 238–245.
[9] N. Pekula, K. Heller, P.A. Chuang, A. Turhan, M.M. Mench, J.S. Brenizer, K. Unlu, Study of water distribution and transport in a polymer electrolyte fuel cell using neutron imaging, Nucl. Instrum. Methods Phys. Res. A 542 (2005) 134–141.
[10] D. Kramer, J. Zhang, R. Shimoi, E. Lehmann, A. Wokaun, K. Shinohara, G.G. Scherer, In situ diagnostic of two-phase flow phenomena in polymer electrolyte fuel cells by neutron imaging. Part A. Experimental, data treatment, and quantification, Electrochim. Acta 50 (2005) 2603–2614.
[11] K.W. Feindel, L.P.-A. LaRocque, D. Starke, S.H. Bergens, R.E. Wasylishen, In situ observations of water production and distribution in an operating H2/O2 PEM fuel cell assembly using ^{1}H NMR microscopy, J. Am. Chem. Soc. 126 (2004) 11436.
[12] K.W. Feindel, S.H. Bergens, R.E. Wasylishen, The use of ^{1}H NMR microscopy to study proton-exchange membrane fuel cells, Chem. Phys. Chem. 7 (2006) 67–75.
[13] S. Tsushima, K. Teranishi, S. Hirai, Magnetic resonance imaging of the water distribution within a polymer electrolyte membrane in fuel cells, Electrochem. Solid-State Lett. 7 (2004) A269–A272.
[14] K. Teranishi, S. Tsushima, S. Hirai, Study of the effect of membrane thickness on the performance of polymer electrolyte fuel cells by water distribution in a membrane, Electrochem. Solid-State Lett. 8 (2005) A281–A284.
[15] S. Tsushima, K. Teranishi, K. Nishida, S. Hirai, Water content distribution in a polymer electrolyte membrane for advanced fuel cell system with liquid water supply, Magn. Reson. Imaging 23 (2005) 255–258.
[16] V.M. Ugaz, P.D. Majors, R.W. Miksad, Measurements of electrorheological fluid flow through a rectangular channel using nuclear magnetic resonance imaging, in: Developments in Electrorheological Flows and Measurement Uncertainty FED-205, American Society of Mechanical Engineers, New York, 1994, pp. 15–27.
[17] M. Zweckstetter, T.A. Holack, An adiabatic multiple spin–echo pulse sequence: removal of systematic errors due to pulse imperfections and off-resonance effects, J. Magn. Reson. 133 (1998) 134–147.
[18] H. Lei, J. Dunn, The effects of slice-selective excitation/refocusing in localized spectral editing with gradient-selected double-quantum coherence transfer, J. Magn. Reson. 150 (2001) 17–25.
[19] P.T. Callaghan, Principles of Nuclear Magnetic Resonance Microscopy, Oxford University Press, New York, 1993.
[20] J.M. Pope, Application of chemical shift microscopy to non-invasive histochemistry of plant materials, in: Blumich Bernhard, Kuhn Winfried (Eds.), Magnetic Resonance Microscopy: Methods And Applications In Materials Science Agriculture And Biomedicine, VCH Publishers, New York, NY (USA), 1992.
[21] F.D. Doty, G. Entzminger, Y.A. Yang, Magnetism in high-resolution NMR probe design. I: general methods, Concepts Magn. Reson. 10 (1998) 133–156.
[22] A.R. von Hippel, Dielectric Properties and Waves, John Wiley, New York, 1954.
[23] See, for example, http://www.magnevu.com/contact.html for a typical low-cost, low-field MRI system and http://www.sai1.net/MRI%20Specifications.htm for related specifications.